CORA Cork Open Research Archive
Cartlann Taighde Oscailte Chorcaí

Title	Intervalence band solitary waves in semiconductor quantum wells
Authors	Biancalana, Fabio;Healy, Sorcha B.;Fehse, Robin;O'Reilly, Eoin P.
Publication date	2006
Original Citation	Biancalana, F., Healy, S. B., Fehse, R. and O'Reilly, E. P. (2006) 'Intervalence band solitary waves in semiconductor quantum wells', Physical Review A, 73(6), 063826 (13pp). doi: 10.1103/PhysRevA.73.063826
Type of publication	Article (peer-reviewed)
Link to publisher's version	https://journals.aps.org/pra/abstract/10.1103/PhysRevA.73.063826 - 10.1103/PhysRevA.73.063826
Rights	© 2006, American Physical Society
Download date	2023-05-05 10:35:33
Item downloaded from	http://hdl.handle.net/10468/4554

UCC
University College Cork, Ireland
Coláiste na hOllscoile Corcaigh

Intervalence band solitary waves in semiconductor quantum wells

Fabio Biancalana,* Sorcha B. Healy, Robin Fehse, and Eoin P. O'Reilly
Tyndall National Institute, Lee Maltings, Cork, Ireland
(Received 15 February 2006; published 28 June 2006)

We show theoretically the possibility of excitation of a special class of two-frequency solitons, sustained by the nonlinearity provided by the nonradiative intervalence band coherence between heavy-hole and light-hole excitonic transitions in semiconductor quantum wells. The formation of such resonant solitons excited by femtosecond pulses in $In_xGa_{1-x}As_yP_{1-y}$ quantum wells is investigated numerically using a phenomenological model based on the local-field approximation, and a realistic configuration for their experimental observation is proposed. The pumping conditions for using complex resonant soliton dynamics as an efficient source of continuum generation are also discussed.

DOI: 10.1103/PhysRevA.73.063826 PACS number(s): 42.65.Re, 42.50.Md, 42.65.Tg

I. INTRODUCTION

The comparative study of coherent optical processes existing in semiconductors and those exhibited by dilute media (such as atomic vapors) represents an excellent tool for addressing the fundamental issue of how Coulomb interactions and correlation effects affect the dynamics of coherent quantum optics in a many-body system [1]. The analogies between coherent nonlinear phenomena in atomic two-level systems (2LS's) [2] and two-band semiconductor models have been successfully exploited over the years. Among various effects that have been considered in the literature, of particular importance are photon echo [3], Rabi oscillations [4], and optical Stark shift [5]. For what concerns soliton theory, the discovery of self-induced transparency (SIT) in gaseous media led to spectacular advances in the theoretical understanding of the features of resonant solitons [6]. The direct analog of the SIT phenomenon in semiconductors is the so-called exciton-polariton soliton [7], a nonlinear self-localized wave that resides on the exciton resonance of a two-band optical transition, the properties of which are very well known in the literature [8].

More recently, the investigation of the rich physics of three-level systems (3LS's) in diluite media has revealed the existence of several typical and potentially useful effects such as lasing without inversion [9], electromagnetically induced transparency (EIT) [10], adiabatic population transfer [11], and ultraslow light propagation [12]. As a consequence, several studies can be found in the literature focusing on exploiting the analogy between atomic 3LS's and semiconductor heterostructures with a band structure similar to that of Fig. 1(a) [13].

However, although much is known of the physics of solitary waves supported by nonresonant material excitation of 3LS's (see, e.g., Refs. [14]), there are still several unexplored possibilities for what concerns resonant excitations, the prototype of which is the Raman process, where two of the three levels are not directly coupled in the dipole approximation. In dilute systems, the excitation of the 3LS's by means of a two-photon transition makes possible the indirect excitation of the polarization between the two initially uncoupled energy levels. In this sense, two-photon Raman-like transitions can be understood as a natural extension of the SIT process. In semiconductors, the same concept applies to structures which present a three-band system, such as the ones considered here. The role of Raman nonradiative coherence is played by the so-called intervalence band coherence, the existence and excitability of which have been established in many experimental works [13].

In the present paper we wish to extend the above analogy by considering a special class of solitary waves that Kaplan and co-workers have recently shown analytically to exist in nonlinear gaseous media which exhibit a Raman-like 3LS structure [15]. Other theoretical and numerical aspects of the solitons of Kaplan *et al.* are covered in Refs. [16,17]. We shall establish the physical conditions of the existence and the excitability of intervalence band solitons in $In_xGa_{1-x}As_yP_{1-y}$ semiconductor quantum wells, with a special stress on the physical powers and pulse durations required for a possible experimental verification.

The structure of the paper is the following. In Sec. II a detailed derivation of the Maxwell-Bloch equations of our problem is given, and useful and reasonable approximations

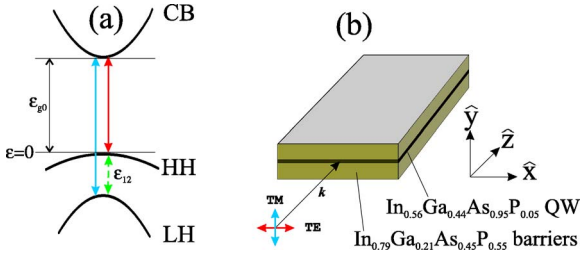

FIG. 1. (Color online) (a) Schematic representation of the three-band semiconductor quantum well. Radiative (nonradiative) transitions are indicated by solid (dashed) arrows. ϵ_{g0} is the band-gap energy; ϵ_{12} is the nonradiative transition energy. More details on this schematic band structure can be found in standard textbooks; see, e.g., [18,19]. (b) Launching configuration proposed in the text (Sec. V). Light is injected with the wave vector k parallel to the plane of the QW. The two polarizations (TE and TM) are also shown. This configuration is preferred due to the relatively long propagation distances, of the order of millimeters, necessary to observe the soliton formation.

*Electronic address: fbianca@tyndall.ie

 ©2006 The American Physical Society

are made in order to simplify drastically the numerical treatment. In Sec. III we find the numerical solutions of the associated boundary value problem and classify rigorously the soliton solutions according to the only free parameter of the system: i.e., the group velocity of the soliton. Numerical propagation is also presented, which shows the stability and conditions for the excitation of the solitary wave under study. Section IV is devoted to the analysis of a spectral continuum due to excitation by double pumping. Finally, in Sec. V we propose a specific structure that satisfies most of the requirements explained in Sec. II.

II. GOVERNING EQUATIONS

Let us consider a type-I semiconductor quantum well (QW) with a band structure similar to that of Fig. 1(a), which can be described in terms of a single conduction band (CB) and two valence bands—respectively, one heavy-hole (HH) band and one light-hole (LH) band. Coherence between different bands can be induced by injecting light pulses with frequencies close to the transition frequencies between the valence bands and the conduction band. The dipole transitions between LH and CB and between HH and CB are allowed under specific polarization conditions for the pulses (selection rules) that depend on the experimental configuration. The direct optical transition from the LH band to the HH band is forbidden for a broad range of wave vectors, and coherence between these two valence bands can be efficiently induced only indirectly by a two-photon, Raman-like process. If the LH-HH splitting is sufficiently large, but still several times smaller than the CB-LH and CB-HH energy separations, the transfer of the hole population between the $|\mathrm{LH}\rangle$ state and the $|\mathrm{HH}\rangle$ state can occur by means of an intermediate transition through the $|\mathrm{CB}\rangle$ state, as indicated by the arrows in Fig. 1(a). This process can be seen as the semiconductor analog of the well-known Raman effect in atomic 3LS physics [20]. The important difference is that, whereas in atomic 3LS the nonradiative coherence is theoretically very well understood, the theoretical and experimental analysis of such coherence in semiconductors (also called *intervalence band coherence*, IVB for brevity) is strongly influenced by many-body processes which may alter the dynamics substantially [1]. This is a consequence of the fact that free LH and HH excitons in QW's cannot be treated as a simple collection of bare 3LS's, since they are all coupled by the long-range Coulomb interaction.

We start from the microscopic Hamiltonian constructed by taking into account all possible interactions between the quasielectrons in the electron representation, and we use the Hartree-Fock (HF) approximation in the semiconductor Bloch equations (SBE's [29]) to truncate the infinite hierarchy of differential equations arising from the Liouville equations of motion for the density matrix ρ [30]. It is therefore possible to show that one obtains the following *effective* Hamiltonian (from now on the overbar shall indicate complex conjugation):

$$H^{\mathrm{eff}} = \hbar \sum_{\mathbf{k}} \begin{bmatrix} \omega_{\mathbf{k}}^{e} & -\Omega_{1,\mathbf{k}} & -\Omega_{2,\mathbf{k}} \\ -\bar{\Omega}_{1,\mathbf{k}} & -\omega_{\mathbf{k}}^{h1} & -\sum_{\mathbf{q}\neq 0} v_{\mathbf{q}} Q_{\mathbf{k}-\mathbf{q}} \\ -\bar{\Omega}_{2,\mathbf{k}} & -\sum_{\mathbf{q}\neq 0} v_{\mathbf{q}} \bar{Q}_{\mathbf{k}-\mathbf{q}} & -\omega_{\mathbf{k}}^{h2} \end{bmatrix}. \tag{1}$$

Here $\mathbf{k}$ is the electronic momentum. Vector quantities shall be indicated from now on by bold letters. $\hbar\omega_{\mathbf{k}}^{e/hj}$ are the renormalized energies for electrons and holes, defined by

$$\omega_{\mathbf{k}}^{e} \equiv \frac{1}{\hbar}\epsilon_{\mathbf{k}}^{e} - \sum_{\mathbf{q}\neq 0} v_{\mathbf{q}} n_{\mathbf{k}-\mathbf{q}}^{e}, \tag{2}$$

$$\omega_{\mathbf{k}}^{hj} \equiv \frac{1}{\hbar}\epsilon_{\mathbf{k}}^{hj} + \sum_{\mathbf{q}\neq 0} v_{\mathbf{q}} (1 - n_{\mathbf{k}-\mathbf{q}}^{hj}), \tag{3}$$

where $n_{\mathbf{k}}^{e/hj}$ are, respectively, the electron and hole occupation numbers. $v_{\mathbf{q}} \equiv V_{\mathbf{q}}/\hbar$, where $V_{\mathbf{q}}$ is the quantum well Coulomb potential in momentum space. Indices $j=1,2$ correspond to the $|\mathrm{HH}\rangle$ and $|\mathrm{LH}\rangle$ states, respectively. The nonrenormalized energies are, respectively, $\epsilon_{\mathbf{k}}^{e} \equiv \epsilon_{g0} + \hbar^2\mathbf{k}^2/(2m_e)$, $\epsilon_{\mathbf{k}}^{h1} \equiv \hbar^2\mathbf{k}^2/(2m_{h1})$, and $\epsilon_{\mathbf{k}}^{h2} \equiv \epsilon_{12} + \hbar^2\mathbf{k}^2/(2m_{h2})$, where $m_e > 0$ and $m_{hj} > 0$ are the effective masses of the quasielectrons in the conduction band and of the holes in the two valence bands, respectively, ϵ_{g0} is the unrenormalized band-gap energy, and ϵ_{12} is the LH-HH energy splitting [see Fig. 1(a)]. In the following calculations we assume for simplicity that the linear optical response is dominated by $1s$-LH and $1s$-HH excitons.

$\Omega_{1,\mathbf{k}}$ and $\Omega_{2,\mathbf{k}}$ are the renormalized total Rabi frequencies associated with the *total* (real) electric field $\mathbf{E}(z,t)$, for the two direct dipole transitions [$j=1,2$; see the solid arrows in Fig. 1(a)], defined by

$$\Omega_{j,\mathbf{k}} \equiv \frac{1}{\hbar}\mathbf{d}_{\mathbf{k}}^{(j)} \cdot \mathbf{E}(z,t) + \sum_{\mathbf{q}\neq 0} v_{\mathbf{q}} p_{j,\mathbf{k}-\mathbf{q}}, \tag{4}$$

where $p_{j,\mathbf{k}}$ are complex matrix elements for the transitions HH-CB ($j=1$) and LH-CB ($j=2$), proportional to the polarization fields for those transitions, and $\mathbf{d}_{\mathbf{k}}^{(j)}$ are the associated dipole moments. $Q_{\mathbf{k}}$ is the nonradiative IVB matrix element for the polarization between the levels $|\mathrm{LH}\rangle$ and $|\mathrm{HH}\rangle$, the structure of which we shall consider further below. A quantity which is also useful to define for future use is the unrenormalized total Rabi frequency: $\Theta_{j,\mathbf{k}} \equiv \mathbf{d}_{\mathbf{k}}^{(j)} \cdot \mathbf{E}/\hbar$. In order to avoid any confusion with our terminology and to conform to the notation used in many textbooks [cf. [19], Eq. (3.21)] and in the literature, it is important to note that the $\Theta_{j,\mathbf{k}}$ are defined using the *total* electric field, and not just one of its frequency components, due to the fact that we have not yet performed any particular approximation to decompose the different frequencies of the electric field. This will be done explicitly later in Eq. (22). We have considered only vertical transitions, since the photon momentum is negligible in comparison to the electronic one. The electric field $\mathbf{E}$ and the dipole moment $\mathbf{d}$ are of course vector quantities. It is important to note that the scalar product between $\mathbf{d}$ and $\mathbf{E}$ in the

above definitions of $\Omega_{\mathbf{k}}$ and $\Theta_{\mathbf{k}}$ encodes all the relevant information on the polarization state of the light and the material. This scalar product will remain implicit unless a polarization basis is chosen and a geometry for the experiment is selected, as discussed further in Sec. V.

The HF Hamiltonian (1) gives the correct description of the excitonic effects in the absence of phonons and other decoherence phenomena, which are typically introduced in a phenomenological way at the end of the derivation [21]. In deriving Eq. (1), we have neglected the precise details of the valence band structure due to the Luttinger Hamiltonian [22], which in a more rigorous approach must be included and which are necessary for a more quantitative discussion [23]. However, we are interested here in a qualitative and semiquantitative understanding of IVB solitons, which are not affected by the precise structure of the valence bands, so that in our treatment we assume the valence band to be of parabolic shape and the HH-LH splitting to be sufficiently large in order to minimize the effects of band coupling. A more detailed discussion of the validity of the above assumptions concerning the band structure is presented in Sec. V.

The expectation value of the density matrix for the problem is given, for each momentum $\mathbf{k}$, by the 3×3 matrix

$$\langle \rho_{\mathbf{k}} \rangle = \begin{bmatrix} n_{\mathbf{k}}^{e} & p_{1,\mathbf{k}} & p_{2,\mathbf{k}} \\ \bar{p}_{1,\mathbf{k}} & 1-n_{\mathbf{k}}^{h1} & Q_{\mathbf{k}} \\ \bar{p}_{2,\mathbf{k}} & \bar{Q}_{\mathbf{k}} & 1-n_{\mathbf{k}}^{h2} \end{bmatrix}, \tag{5}$$

supported by the condition of conservation of total probability for each three-level subsystem—namely, $\mathrm{Tr}(\langle \rho_{\mathbf{k}} \rangle)=2$ or, in other words, $n_{\mathbf{k}}^{h1}+n_{\mathbf{k}}^{h2}-n_{\mathbf{k}}^{e}=0$. As we shall see shortly, if the latter condition is satisfied for an arbitrary time $t=t'$, then it must hold for all times $t>0$. Thus the trace condition is an initial condition for the number of particles initially present in the system. The value of the trace follows from the structure of the QW ground state, with both valence bands filled at zero temperature. Importantly, this is in contrast with the ground-state structure of an atomic 3LS, for which generally only the lowest-energy state is populated at low temperatures. In Eq. (5) we have defined the following expectation values from the annihilation and creation operators for a specified momentum $\mathbf{k}$ in the electron ($\{a_{\mathbf{k}}, a_{\mathbf{k}}^{\dagger}\}$) and hole ($\{b_{j,-\mathbf{k}}, b_{j,-\mathbf{k}}^{\dagger}\}$) representations [19,21,24,26]:

$$\langle a_{\mathbf{k}}^{\dagger} a_{\mathbf{k}} \rangle \equiv n_{\mathbf{k}}^{e}, \quad \langle b_{j,-\mathbf{k}}^{\dagger} b_{j,-\mathbf{k}} \rangle \equiv n_{\mathbf{k}}^{hj},$$

$$\langle b_{j,-\mathbf{k}} a_{\mathbf{k}} \rangle \equiv p_{j,\mathbf{k}}, \quad \langle b_{1,-\mathbf{k}}^{\dagger} b_{2,-\mathbf{k}} \rangle \equiv -Q_{\mathbf{k}}. \tag{6}$$

The total density matrix is defined as $\rho \equiv \Sigma_{\{\mathbf{k}\}} \rho_{\mathbf{k}}$, where with the generic symbol $\Sigma_{\{\mathbf{k}\}}$ we indicate a sum over the density of states in momentum space (normalized over the total carrier density) which depends on the precise details of the band structure, the dimensionality of the problem, and all possible additional degrees of freedom (like spin where necessary) [18,21]. Note that the fundamental condition $\mathrm{Tr}(\langle \rho \rangle)=1$ must always hold.

The next step is to obtain equations for all the elements of the density matrix—i.e., for all the dynamical variables of the problem. For this purpose we use the Liouville equation $i\hbar \partial_t \langle \rho_{\mathbf{k}} \rangle = \langle [H^{\mathrm{eff}}, \rho_{\mathbf{k}}] \rangle$, which yields the following set of equations:

$$\partial_t n_{\mathbf{k}}^{e} + 2\,\mathrm{Im}\left(\sum_j \Omega_{j,\mathbf{k}} \bar{p}_{j,\mathbf{k}} \right) = 0, \tag{7}$$

$$\partial_t n_{\mathbf{k}}^{h1} + 2\,\mathrm{Im}\left(\Omega_{1,\mathbf{k}} \bar{p}_{1,\mathbf{k}} + \sum_{\mathbf{q}\neq 0} v_{\mathbf{q}} \bar{Q}_{\mathbf{k}-\mathbf{q}} Q_{\mathbf{k}} \right) = 0, \tag{8}$$

$$\partial_t n_{\mathbf{k}}^{h2} + 2\,\mathrm{Im}\left(\Omega_{2,\mathbf{k}} \bar{p}_{2,\mathbf{k}} + \sum_{\mathbf{q}\neq 0} v_{\mathbf{q}} Q_{\mathbf{k}-\mathbf{q}} \bar{Q}_{\mathbf{k}} \right) = 0, \tag{9}$$

$$i\partial_t p_{1,\mathbf{k}} - (\omega_{\mathbf{k}}^{e} + \omega_{\mathbf{k}}^{h1}) p_{1,\mathbf{k}} + \Omega_{1,\mathbf{k}} (1 - n_{\mathbf{k}}^{h1} - n_{\mathbf{k}}^{e}) - \left(\sum_{\mathbf{q}\neq 0} v_{\mathbf{q}} \bar{Q}_{\mathbf{k}-\mathbf{q}} \right) p_{2,\mathbf{k}} + \Omega_{2,\mathbf{k}} \bar{Q}_{\mathbf{k}} = 0, \tag{10}$$

$$i\partial_t p_{2,\mathbf{k}} - (\omega_{\mathbf{k}}^{e} + \omega_{\mathbf{k}}^{h2}) p_{2,\mathbf{k}} + \Omega_{2,\mathbf{k}} (1 - n_{\mathbf{k}}^{h2} - n_{\mathbf{k}}^{e}) - \left(\sum_{\mathbf{q}\neq 0} v_{\mathbf{q}} Q_{\mathbf{k}-\mathbf{q}} \right) p_{1,\mathbf{k}} + \Omega_{1,\mathbf{k}} Q_{\mathbf{k}} = 0, \tag{11}$$

$$i\partial_t Q_{\mathbf{k}} + (\omega_{\mathbf{k}}^{h1} - \omega_{\mathbf{k}}^{h2}) Q_{\mathbf{k}} - [\Omega_{2\mathbf{k}} \bar{p}_{1\mathbf{k}} - \bar{\Omega}_{1\mathbf{k}} p_{2\mathbf{k}}] + \left(\sum_{\mathbf{q}\neq 0} v_{\mathbf{q}} Q_{\mathbf{k}-\mathbf{q}} \right) \times (n_{\mathbf{k}}^{h1} - n_{\mathbf{k}}^{h2}) = 0, \tag{12}$$

supported by the initial condition

$$[-n_{\mathbf{k}}^{e} + n_{\mathbf{k}}^{h1} + n_{\mathbf{k}}^{h2}]_{t=t'} = 0, \tag{13}$$

valid for some arbitrary time $t=t'$. The constancy in time of the quantity in the square brackets in Eq. (13) is ensured by Eqs. (7)–(9)

In general, in a quantum transition where N photons are exchanged through $N+1$ eigenstates of the unexcited medium (N is called the *order* of the transition), one has $(N+1)(N+2)/2$ equations for the components of the density matrix, plus one initial condition given by the trace of the density matrix. In our particular case $N=2$ (the nonradiative transition is excited by two photons) and we have $(2+1)(2+2)/2=6$ equations, given by Eqs. (7)–(12). Equation (13) gives the condition $\mathrm{Tr}(\langle \rho_{\mathbf{k}} \rangle)=2$. The terms in Eqs. (10) and (11) proportional to $(1-n_{\mathbf{k}}^{h1,2}-n_{\mathbf{k}}^{e})$ determine the intensity of the dipole coupling between light and electron-hole pairs in the semiconductor.

The set of equations reported above provides the most general Bloch-like equations for the problem of two-photon transitions in a QW which is possible to obtain from the HF approximation, when neglecting the detailed structure (due to band coupling) of the valence bands and when assuming that the material and the optical fields interact in the framework of the dipole moment approximation. Unfortunately an accurate numerical solution of Eqs. (7)–(13) would be very demanding even for modern workstations [25,26]. Therefore other approximations are necessary in order to reduce their complexity.

First of all we assume that the renormalized transition frequencies $\omega_{j,\mathbf{k}} \equiv \omega_{\mathbf{k}}^{e} + \omega_{\mathbf{k}}^{hj}$, which appear in Eqs. (10) and (11), are much larger than the LH-HH splitting frequency, given by $\omega_{12} \equiv \epsilon_{12}/\hbar > 0$. This is certainly true for InGaAsP

QW's, and it represents an excellent approximation for many materials and geometries; see also Sec. V for further clarification of this point. As a consequence of this assumption, one can neglect the temporal derivatives in Eqs. (10) and (11), posing $\partial_t p_{j,\mathbf{k}} \simeq 0$ in these equations. In this way the complex polarizations $p_{1,\mathbf{k}}$ and $p_{2,\mathbf{k}}$ can be expressed in terms of the other dynamical variables, reducing the number of independent dynamical variables by two units. However, one cannot solve Eqs. (10) and (11) in the variables $p_{j,\mathbf{k}}$ immediately after posing $\partial_t p_{j,\mathbf{k}} \simeq 0$, since the renormalized total Rabi frequencies $\Omega_{j,\mathbf{k}}$ depend on all $p_{j,\mathbf{k}}$'s due to the Coulomb contribution contained in Eq. (4). It follows that one must therefore neglect the Coulomb renormalization in Eqs. (10) and (11) in order to extract a closed expression for the $p_{j,\mathbf{k}}$. It is possible to show that further simplifications of the expressions for $p_{j,\mathbf{k}}$ are achieved by considering that $|\Sigma_{q\neq 0} v_{\mathbf{q}} Q_{\mathbf{k}-\mathbf{q}}| \ll \omega_{j,\mathbf{k}}$. Moreover, it will be useful for our purposes to consider only those fields for which the unrenormalized total Rabi frequencies are much smaller than the transition frequencies, $|\Theta_{j,\mathbf{k}}| \ll \omega_{j,\mathbf{k}}$; this will pose a (weak) condition on the physical intensities of the light pulses (see also [27], Chap. 7), and it avoids the appearance of small nonlinear renormalization terms in the expressions for $p_{j,\mathbf{k}}$. With these approximations one finally obtains

$$p_{1,\mathbf{k}} \simeq \frac{1}{\omega_{\mathbf{k}}}[\Theta_{2,\mathbf{k}} \bar{Q}_{\mathbf{k}} + \Theta_{1,\mathbf{k}}(1 - n_{\mathbf{k}}^{h1} - n_{\mathbf{k}}^{e})], \tag{14}$$

$$p_{2,\mathbf{k}} \simeq \frac{1}{\omega_{\mathbf{k}}}[\Theta_{1,\mathbf{k}} Q_{\mathbf{k}} + \Theta_{2,\mathbf{k}}(1 - n_{\mathbf{k}}^{h2} - n_{\mathbf{k}}^{e})], \tag{15}$$

where $\omega_{\mathbf{k}} \equiv (\omega_{1,\mathbf{k}} \omega_{2,\mathbf{k}})^{1/2}$.

The second important simplification which is possible to impose comes from the circumstance that, during the two-photon process—which is second order in the perturbation theory due to the fact that the direct optical transition between the $|\mathrm{LH}\rangle$ band and the $|\mathrm{HH}\rangle$ band is largely forbidden—the $|\mathrm{CB}\rangle$ band does not undergo an appreciable change in population. This follows directly from substituting Eqs. (14) and (15) into Eq. (7). This means that the levels in the conduction band can be considered as spectators during the process, and one can therefore pose $\partial_t n_{\mathbf{k}}^{e} \simeq 0$, which means $n_{\mathbf{k}}^{e} \simeq$ const, in the same approximations used to derive Eqs. (14) and (15). It is important to note that this constant must be positive and cannot be zero. This follows from the fact that $n_{\mathbf{k}}^{h1,2}$ and $n_{\mathbf{k}}^{e}$ are all real positive numbers and that $n_{\mathbf{k}}^{h1} + n_{\mathbf{k}}^{h2} \neq 0$ implies that $n_{\mathbf{k}}^{e} \neq 0$. Applying this approximate constancy condition to Eq. (13) one immediately obtains that $n_{\mathbf{k}}^{h1} \simeq n_{\mathbf{k}}^{e} - n_{\mathbf{k}}^{h2}$. Defining the renormalized hole density difference $n_{\mathbf{k}} \equiv (n_{\mathbf{k}}^{h1} - n_{\mathbf{k}}^{h2})/n_{\mathbf{k}}^{e}$, we can then use the "inversion" $-1 \leq n_{\mathbf{k}} \leq +1$ as dynamical variable, associated with the two further scalings $\Theta_{1,2,\mathbf{k}} \to \Theta_{1,2,\mathbf{k}}/(n_{\mathbf{k}}^{e})^{1/2}$ and $v_{\mathbf{k}} \to v_{\mathbf{k}}/n_{\mathbf{k}}^{e}$. Note that, in the new notation, when the $|\mathrm{LH}\rangle$ state and $|\mathrm{HH}\rangle$ state have an equal population of *holes*, we then have that $n_{\mathbf{k}} = 0$. Such a state can be reached in principle by preparing the semiconductor coherently by pumping optically the electrons from the $|\mathrm{HH}\rangle$ and $|\mathrm{LH}\rangle$ bands to the conduction band $|\mathrm{CB}\rangle$; see Sec. V for a brief discussions of this point. The soliton formation that we are going to describe in the following and, more importantly, the type of solitons which are possible to excite in the material are strongly affected by the precise boundary conditions for the population field. An initially equal population of holes present in the $|\mathrm{HH}\rangle$ and $|\mathrm{LH}\rangle$ states can be transferred from one level to another by means of a dipole interaction with the optical fields; the efficiency of this process depends on how many dipoles are present initially in the semiconductor, and the number of dipoles can be directly related to the exciton density.

Finally, it must be noted that with all previous simplifications the condition $\mathrm{Im}(\Sigma_j \Omega_{j,\mathbf{k}} \bar{p}_{j,\mathbf{k}}) = 0$, derived from Eq. (7), is automatically satisfied; this corresponds to a no-absorption law on the conduction band during the two-photon process.

Under the above conditions, using Eq. (12), combining Eqs. (8) and (9), and eliminating $p_{j,\mathbf{k}}$ by using the relations (14) and (15), one obtains the following set of equations for the relative LH-HH hole population $n_{\mathbf{k}}$ and the IVB coherence field $Q_{\mathbf{k}}$:

$$i\partial_t Q_{\mathbf{k}} - \left(\Delta\omega_{\mathbf{k}} + \frac{|\Theta_{2,\mathbf{k}}|^2 - |\Theta_{1,\mathbf{k}}|^2}{\omega_{\mathbf{k}}} + \sum_{\mathbf{q}\neq 0} v_{\mathbf{q}} n_{\mathbf{k}-\mathbf{q}} \right) Q_{\mathbf{k}} + \left(\frac{\Theta_{1,\mathbf{k}} \bar{\Theta}_{2,\mathbf{k}}}{\omega_{\mathbf{k}}} + \sum_{\mathbf{q}\neq 0} v_{\mathbf{q}} Q_{\mathbf{k}-\mathbf{q}} \right) n_{\mathbf{k}} = 0, \tag{16}$$

$$\partial_t n_{\mathbf{k}} + 4\,\mathrm{Im}\left(\left[\frac{\bar{\Theta}_{1,\mathbf{k}} \Theta_{2,\mathbf{k}}}{\omega_{\mathbf{k}}} + \sum_{\mathbf{q}\neq 0} v_{\mathbf{q}} \bar{Q}_{\mathbf{k}-\mathbf{q}} \right] Q_{\mathbf{k}} \right) = 0, \tag{17}$$

where $\Delta\omega_{\mathbf{k}} \equiv (\epsilon_{\mathbf{k}}^{h2} - \epsilon_{\mathbf{k}}^{h1})/\hbar$. Conservation of probability results in the relation $n_{\mathbf{k}}^2 + 4|Q_{\mathbf{k}}|^2 \simeq \mathrm{Tr}(\langle \rho_{\mathbf{k}} \rangle)^2 = 4$, valid for all values of $\mathbf{k}$ and at all times in the absence of decoherence processes.

It is of crucial importance to note that Eqs. (16) and (17) have the same structure as the Bloch equations for a set of *effective* two-level systems, represented by the valence bands $|\mathrm{LH}\rangle$ and $|\mathrm{HH}\rangle$ for all values of $\mathbf{k}$, and the conduction band has been completely decoupled from the dynamics, thanks to the approximate constancy of $n_{\mathbf{k}}^{e}$ derived above. The obvious difference with the optical Bloch equations (OBE's) of a set of inhomogeneously broadened oscillators is, however, that the renormalization terms proportional to $v_{\mathbf{q}}$ contained in Eqs. (16) and (17) couple all Raman-like oscillators to each other. Nevertheless the complexity of these equations is considerably reduced with respect to the full equations (7)–(13).

Equations (16) and (17) model the response of the material when excited by the electric field $\mathbf{E}(z,t)$, contained inside $\Theta_{\mathbf{k}}$. The propagation is assumed to be one dimensional, with z being the longitudinal coordinate along which propagation occurs. We now need to write an equation for $\mathbf{E}$, when coupled to the material oscillators $Q_{\mathbf{k}}$'s. This is the reduced (forward) version of the Maxwell wave equation, which we write as [23,25]

$$i[\partial_z + \beta'(\omega)]\mathbf{E} + \frac{\omega^2}{2\beta(\omega)\epsilon_0 c^2} \mathbf{P}_{tot} = 0, \tag{18}$$

where $\mathbf{P}_{tot}$ is the total polarization exhibited by the medium when in resonance with the IVB coherence, $\beta(\omega) = n(\omega)\omega/c$ is the optical wave vector, $n(\omega)$ is the refractive

index at the frequency ω exhibited by the waveguide structure, c is the speed of light in vacuum, and the prime indicates a derivative with respect to the optical frequency ω.

An essential ingredient of Eq. (18) is the total polarization $\mathbf{P}_{tot}$, which must be a real quantity. To find it, we need to use the quantum mechanical average

$$\mathbf{P}_{tot} \equiv \sum_{\{\mathbf{k}\}} \mathrm{Tr}(\hat{\mathbf{d}}_{\mathbf{k}} \rho_{\mathbf{k}}), \tag{19}$$

where $\hat{\mathbf{d}}_{\mathbf{k}}$ is the dipole operator given by

$$\hat{\mathbf{d}}_{\mathbf{k}} = \begin{pmatrix} 0 & \mathbf{d}_{\mathbf{k}}^{(1)} & \mathbf{d}_{\mathbf{k}}^{(2)} \\ \mathbf{d}_{\mathbf{k}}^{(1)} & 0 & 0 \\ \mathbf{d}_{\mathbf{k}}^{(2)} & 0 & 0 \end{pmatrix}. \tag{20}$$

$\hat{\mathbf{d}}_{\mathbf{k}}$ contains a vanishing 2×2 submatrix since there is no direct dipole coupling between the two valence bands. This assertion will be fully justified in Sec. V, where the band structure and dipole matrix elements of the relevant transitions for a realistic QW will be calculated. If one poses for simplicity $\mathbf{d}_{\mathbf{k}}^{(1)} \simeq \mathbf{d}_{\mathbf{k}}^{(2)} \equiv \mathbf{d}_{\mathbf{k}}$, so that $\Theta_{1,\mathbf{k}} \simeq \Theta_{2,\mathbf{k}} \equiv \Theta_{\mathbf{k}}$, we obtain the expression

$$\begin{aligned} \mathbf{P}_{tot} &\simeq 2\sum_{\{\mathbf{k}\}} \mathbf{d}_{\mathbf{k}} \,\mathrm{Re}(p_{1,\mathbf{k}} + p_{2,\mathbf{k}}) \\ &= \frac{4 d_{\mathbf{k}} \tilde{\mathbf{d}}}{\hbar \omega_{\mathbf{k}}} \sum_{\{\mathbf{k}\}} \mathrm{Re}(E) \left[\mathrm{Re}(Q_{\mathbf{k}}) + \left(1 - \frac{3}{2} n_{\mathbf{k}}^{e}\right) \right], \end{aligned} \tag{21}$$

where in the last expression we have used relations (14) and (15). In Eq. (21) we have defined $\mathbf{d}_{\mathbf{k}} \equiv d_{\mathbf{k}} \cdot \tilde{\mathbf{d}}$, where $\tilde{\mathbf{d}}$ is a unit vector along the polarization direction and $E \equiv \tilde{\mathbf{d}} \cdot \mathbf{E}$. In this last product information on the polarization state of the light is encoded, which then depends on the geometry of the experiment.

The next important step is to use the slowly varying envelope approximation (SVEA) for the electric field $\mathbf{E}(z,t)$ and the rotating-wave approximation (RWA) for the coherence fields $Q_{\mathbf{k}}$. This is done by first writing

$$\mathbf{E} = \frac{1}{2}(\mathbf{E}_P e^{-i\omega_P t} + \mathbf{E}_S e^{-i\omega_S t} + \mathrm{c.c.}), \tag{22}$$

$$Q_{\mathbf{k}} = \frac{1}{2} q_{\mathbf{k}} e^{-i\Delta\omega_{\mathbf{k}} t}, \tag{23}$$

and then neglecting all the second-order derivatives in space and time that appear in the equations for $\mathbf{E}_{P,S}$ [28]. When $\omega_P > \omega_S$, $\mathbf{E}_P$ is called the *pump wave* while $\mathbf{E}_S$ is called the *Stokes wave*, according to the terminology used in atomic Raman 3LS's [20].

In order to progress further, we now wish to work with the *macroscopic* observables associated with the microscopic fields $q_{\mathbf{k}}$ and $n_{\mathbf{k}}$. For this purpose we define the macroscopic interband polarization q and population n as

$$q \equiv \sum_{\{\mathbf{k}\}} q_{\mathbf{k}}, \quad n \equiv \sum_{\{\mathbf{k}\}} n_{\mathbf{k}}. \tag{24}$$

We choose to follow a procedure analogous to the one outlined in Ref. [31], in order to derive a plausible set of phenomenological equations for the set of dynamical variables $\{E_P, E_S, q, n\}$. This procedure consists of two distinct steps, which altogether we shall call "phenomenological reduction." The first step is to substitute Eqs. (22) and (23) into Eqs. (16) and (17) and Eq. (18), regrouping the phase-matched terms and making use of the total material polarization, Eq. (21), in the Maxwell equations. This allows us to write SVEA equations for the electric field envelopes E_P and E_S and RWA equations for the microscopic polarization fields $q_{\mathbf{k}}$ [as defined in Eq. (23)] and populations $n_{\mathbf{k}}$. The second and most important step consists in applying the operator $\Sigma_{\{\mathbf{k}\}}$, which averages out over the density of states in momentum space, onto the Bloch equations (16) and (17), in order to extract equations for the macroscopic observables q and n as defined in Eq. (24). However, this is in general an impossible task to accomplish for all terms in Eqs. (16) and (17) for the simple reason that the factorization of a product of two quantities which both depend on the momentum $\mathbf{k}$ is in general not allowed. This is certainly not surprising, due to the intrinsic many-body nature of the problem. However, assuming a strongly localized nature of the Coulomb potential $v_{\mathbf{q}}$ around $\mathbf{q}=0$, one can justify the following Bowden-Agrawal ansatz [31]:

$$\sum_{\mathbf{q}\neq 0} v_{\mathbf{q}} n_{\mathbf{k}-\mathbf{q}} = \sum_{\mathbf{q}\neq \mathbf{k}} v_{\mathbf{k}-\mathbf{q}} n_{\mathbf{q}} \simeq \mathcal{V} n,$$

where $\mathcal{V} \equiv \Sigma_{\mathbf{q}\neq 0} v_{\mathbf{q}}$ is a coefficient proportional to the Debye shift resulting from band-gap renormalization due to Coulomb-exchange interactions [31,33]. Note that the last member in this ansatz is $\mathbf{k}$ independent. This is reasonable since the main contribution to the sum comes from a narrow, δ-like region in $\mathbf{k}$ space. For further considerations on this approach see, e.g., Eq. (3.68) in Ref. [19] and in particular the works of Ref. [31]. $\mathcal{V}$ physically represents an additional contribution to the band-gap shift; the sign of $\mathcal{V}$ is typically negative, since the screening of a repulsive interaction leads to a decrease of the transition energy with increasing carrier density [19,33], but nevertheless we allow L to be positive to maintain flexibility regarding exotic cases. This point will be discussed further in Sec. III.

With the above prescriptions, the following set of phenomenological equations can be obtained:

$$i\partial_z E_P + i \int \alpha_P(t-t') E_P(t') dt' + i \frac{n_P}{c} \partial_t E_P + \gamma_P q E_S = 0, \tag{25}$$

$$i\partial_z E_S + i \int \alpha_S(t-t') E_S(t') dt' + i \frac{n_S}{c} \partial_t E_S + \gamma_S \bar{q} E_P = 0, \tag{26}$$

$$i\partial_t q + i \frac{1}{T_2} q + (\alpha E_P \bar{E}_S + \mathcal{V} q) n = 0, \tag{27}$$

$$\partial_t n + \frac{1}{T_1}(n - n_0) + \mathrm{Im}([\alpha \bar{E}_P E_S + \bar{\mathcal{V}}\bar{q}]q) = 0, \tag{28}$$

where n_0 is the relaxation value for the population at the QW ground state, which is $n_0 \simeq 0$ in the present case. $\gamma_{P,S} \equiv |\mathbf{d}|^2 N_{3d}/(n_{P,S}\epsilon_0 c\hbar)$ have the dimensions of wave vectors, $\alpha \equiv |\mathbf{d}|^2/(2\hbar^2\omega)$, N_{3d} is the spatial number density of excitons ($N_{3d}=N_{2d}/L_0$, where N_{2d} is the number density of excitons per unit area and L_0 is the well width), ϵ_0 is the permittivity of free space, and $n_{P,S}$ are the refractive indices at the pump and the Stokes frequency. $T_{1,2}$ are two dephasing times, respectively, for the population and coherence field, which must be introduced by hand in our model [24,26,32]. In the absence of dephasing ($T_{1,2} \to +\infty$) and absorption ($\alpha_{P,S} \to 0$), the conservation of probability reads $n^2 + |q|^2 = 1$. $\alpha_{P,S}(t)$ are two response functions which model the frequency-dependent absorption of the QW due to the band structure. The absorption spectra for the pump and the Stokes waves are given by their Fourier transforms $\alpha_{P,S}(\omega)$, and they are also introduced by hand in the model. This is particularly important in applications for continuum generation, where the dynamics are strongly affected by the frequency-dependent absorption; see also Fig. 7(a) and Sec. IV.

The real strong justification for writing phenomenological equations like Eqs. (25)–(28) resides in their successful use in the numerical modeling of a large variety of linear and nonlinear phenomena, which can produce very good qualitative agreement with experiments [31,32]. The phenomenological formulation also has the advantage that it allows many results derived for dense gaseous media to be directly applied to semiconductor physics [8].

Note that the two-photon Rabi frequency renormalization, the excitation-induced dephasing (EID), and the excitation-induced shift (EIS) are present in our effective model through the term proportional to $\mathcal{V}$ in Eq. (27), if one allows $\mathcal{V}$ to be complex. The quantity $\mathrm{Re}(\mathcal{V})n$ represents the EIS effect, which shifts the resonance frequency by an amount which depends on the population field n. The quantity $\mathrm{Im}(\mathcal{V})n$ represents instead the EID effect, which introduces an extra source of dephasing for the field q, to be added to the term proportional to $1/T_2$. Therefore, effectively, the two-photon Rabi frequency renormalization contains both these two effects, which are observable and are well documented in the literature [26]. However, in the following we shall assume $\mathcal{V}$ to be a real parameter for simplicity. The effects associated with an imaginary part of $\mathcal{V}$ described above and associated with extra dephasing effects are not considered. Their detailed treatment can be found elsewhere [32].

III. NUMERICAL RESULTS AND DISCUSSION

Equations (25)–(28) will constitute the starting point of our numerical analysis. First of all, however, it is necessary to rescale the optical fields and the spatial and temporal coordinates, in order to get rid of all the unnecessary coefficients. We use the following scalings:

$$\tau \equiv t/t_0, \quad \xi \equiv z/z_0, \tag{29}$$

$$E_P = \sqrt{\tilde{\alpha}/\kappa}A_P, \quad E_S = \sqrt{\tilde{\alpha}/\kappa}\sqrt{\gamma_S/\gamma_P}A_S, \tag{30}$$

where t_0 and z_0 are temporal and spatial scales that we shall define conveniently shortly, $\tilde{\alpha} \equiv \hbar N_{3d}\omega/\epsilon_0$ and $\kappa \equiv \Delta\beta' c/2$. For values of N_{3d} of the order of 10^{22} carriers/m^{-3}, the scaling factor $\tilde{\alpha}^{1/2}$ for the electric fields is typically of the order of 10^7 V/m. We also introduce a new reference frame moving at the inverse velocity $(n_P+n_S)/(2c) - v_g^{-1}$, where v_g is an arbitrary parameter, the physical meaning of which will be clarified below. We fix the spatial scale to be equal to the first-order dispersion length, $z_0 \equiv t_0/\Delta\beta'$, and the temporal scale to be $t_0 = \Delta\beta'(\gamma_P\gamma_S)^{-1/2}$. We also define the dimensionless parameters $v \equiv z_0 v_g^{-1}/t_0$, $L \equiv \mathcal{V}t_0$, and $\gamma_{1,2} \equiv t_0/T_{1,2}$. With the new rescalings and definitions, Eqs. (25)–(28) become the following set of dimensionless equations, suitable for numerical investigation:

$$i\partial_\xi A_P + i\int \tilde{\alpha}_P(\tau - \tau')A_P(\tau')d\tau' - i(v+1)\partial_\tau A_P + qA_S = 0, \tag{31}$$

$$i\partial_\xi A_S + i\int \tilde{\alpha}_S(\tau - \tau')A_S(\tau')d\tau' - i(v-1)\partial_\tau A_S + \bar{q}A_P = 0, \tag{32}$$

$$i\partial_\tau q + i\gamma_2 q + (A_P\bar{A}_S + Lq)n = 0, \tag{33}$$

$$\partial_\tau n + \gamma_1(n - n_0) + \mathrm{Im}(\bar{A}_P A_S q) = 0, \tag{34}$$

where $\tilde{\alpha}_{P,S} \equiv \alpha_{P,S} z_0$. Cross-phase modulation (XPM) and self-phase modulation (SPM) are neglected in this approach, since one can verify that the contribution of off-resonance nonlinearities in the InGaAsP QW considered in Sec. V is small compared to the strong resonant nonlinearity induced by the IVB coherence.

An interesting property of Eqs. (31)–(34) is the invariance of these equations with respect of the discrete transformation $L \leftrightarrow -L$, $\mathrm{Im}(A_{P,S}) \leftrightarrow -\mathrm{Im}(A_{P,S})$ and $\mathrm{Re}(q) \leftrightarrow -\mathrm{Re}(q)$. This symmetry allows us to adapt all results to the case when L is positive, so that the sign of L is of no importance in the dynamical simulations and the absolute value of the fields and output spectra will be exactly identical in the two cases $L>0$ and $L<0$.

In our dimensionless notation the two-photon Rabi frequency (which essentially represents the driving field in Bloch's equations) is given by the product $\Omega(\xi,\tau) \equiv \bar{A}_P(\xi,\tau)A_S(\xi,\tau)$. We also define the quantity

$$\phi(\xi) \equiv \int_{-\infty}^{+\infty} |\Omega(\xi,\tau)|d\tau. \tag{35}$$

This represents a generalization to a two-photon transition of the pulse area used in SIT [2,6]. Note the use of the absolute value in the definition of Eq. (35).

To extract physical intensities $I_{P,S}$ for the fields (expressed in W/m^2) from the expressions $|A_{P,S}|^2$, one should use the following conversion formula:

$$I_{P,S} = \frac{1}{2} n_{P,S} \epsilon_0 c (\max_t |E_{P,S}|^2)$$
$$= \frac{n_{P,S} \hbar \omega_{P,S} N_{3d}}{\Delta\beta'} (\max_\tau |A_{P,S}|^2)$$
$$\equiv I_0 n_{P,S} (\max_\tau |A_{P,S}|^2). \quad (36)$$

Indicating the physical energies of the two optical components by the symbols $\mathcal{E}_{P,S}$, these are given by

$$\mathcal{E}_{P,S} = \sigma I_{P,S} t_0 A_{\text{eff}}, \quad (37)$$

where σ is a numerical factor which depends on the pulse shape and A_{eff} is the effective area of the incident pulse. The quantities $\mathcal{F}_{P,S} \equiv \mathcal{E}_{P,S}/A_{\text{eff}}$ are the energy fluxes, typically expressed in J/m^2. The corresponding dimensionless energies $B_{P,S}$ can be found by integrating Eq. (36) in time; one finds the following expression:

$$B = \frac{\Delta\beta'}{n_{P,S} \hbar \omega_{P,S} N_{3d} \sigma t_0} \mathcal{F}_{P,S}. \quad (38)$$

It is possible to find the stationary solutions of Eqs. (31)–(34) by solving numerically the associated boundary value problem (BVP), when $\gamma_{1,2} = \tilde{\alpha}_{P,S} = 0$ and L is real. These are of course necessary conditions for the mathematical existence of solitons in the system. Nonvanishing values of $T_{1,2}$, $\alpha_{P,S}$, and $\text{Im}(L)$ will spoil the "stationarity" of the solution, introducing a soliton "lifetime," as will be discussed shortly. $-1 \leqslant v \leqslant +1$ is the only free parameter of the system, and it will serve as a parameter for labeling all the different soliton solutions. When $v=-1$ ($v=+1$) the group velocity of the soliton is equal to the group velocity at the pump (Stokes) frequency ω_P (ω_S). When $L=0$—i.e., in the absence of Coulomb renormalization of the two-photon Rabi frequency—the solution is real and it is known analytically from the work of Kaplan and collaborators [15]. We reproduce it here:

$$A_{P,S}(\tau) = a_{P,S} \sqrt{\text{sech}(\tau/\tau_0)}, \quad (39)$$

$$q(\tau) = -i \tanh(\tau/\tau_0), \quad (40)$$

$$n(\tau) = n_0 \,\text{sech}(\tau/\tau_0), \quad (41)$$

with $a_P = [2/(1+v)]^{1/2}$, $a_S = \pm[2/(1-v)]^{1/2}$, $n_0 = -1$, and $\tau_0 = (1-v^2)^{1/2}/2$. This solution corresponds to solitons with pulse area equal to π. The parameter v determines not only the common velocity of the two optical components, but also it uniquely determines their amplitudes. This physically means that the constraints which the material imposes on the optical fields are so strong that the soliton family possesses only one degree of freedom. This drastic reduction of the number of degrees of freedom in the soliton solutions is typical of SIT-like solitons [6], and the concept can be formulated more quantitatively using the so-called "area theorems" [6,16,34]. It is also important to observe that the physical mechanism which sustains the soliton is the balance between the nonlinearity provided by the IVB coherence and the group velocity mismatch provided by the waveguide. It is particularly interesting to note that, contrary to physical intuition, the greater is the group velocity mismatch between the two optical components, the smaller is the optical intensity necessary to excite the solitary wave, because $\Delta\beta'$ appears in the denominator in Eq. (36) [17]. This is strikingly different from ordinary nonlinear Schrödinger-like equations, in which the soliton existence is due to a balance between the nonlinearity and the group velocity *dispersion* (GVD) of the waveguide [15,16], and can be attributed to the unconventional "gaplike" features of the Raman resonant solitary waves, as first identified in Ref. [17].

However, for $L \neq 0$ the solution is intrinsically complex and can only be found numerically, due to the nontrivial dependence of the complex phase on the population field n.

Examples of the soliton profiles for the pump (A_P) and Stokes (A_S) waves for some specific values of the parameters v and L as calculated numerically are shown in Figs. 2(a) ($v=0.3$ and $L=-0.4$) and 2(d) ($v=0.3$ and $L=+5$). Physically relevant semiconductor solitons possess a profile of the *absolute value* which is very close to the expression of Eq. (39), due to the specific nature of the boundary conditions imposed by the initial state of the semiconductor. Other types of solutions relevant to the case of atomic 3LS's in Raman cells or hollow-core photonic crystal fibers are discussed in Refs. [15–17] and include, for instance, rather unconventional profiles proportional to the square root of a Lorentzian function, as in the case of hollow-core fibers [16].

It can be seen from Figs. 2(a) and 2(d) that for a nonvanishing value of L the two optical fields $A_{P,S}$ acquire imaginary parts of opposite signs, shown with dashed lines in the figures. In Figs. 2(b) and 2(e) the macroscopic polarization field q and the population difference n in correspondence with the solitary-wave solution considered in Figs. 2(a) and 2(d), respectively, are shown. The population starts from a value $n(\tau=-\infty)=0$, which in our notation means that the LH band and HH band have an equal population of holes; see also Fig. 1(a) and caption. In correspondence with the soliton center ($\tau=0$), the population undergoes temporary partial inversion, the extent of which depends on the value of the parameter L, and comes back to the original condition for $\tau \to +\infty$. For $L=0$ the inversion of population is total at $\tau=0$. Larger values of $|L|$ imply smaller values of $|n|$ at the soliton center, as is evident from comparing Fig. 2(b) with Fig. 2(e). It is also interesting to observe the evolution of the coherence field q during the soliton transit [blue lines in Figs. 2(b) and 2(e)]. In order to sustain the resonant soliton, the coherence field must assume a nonvanishing value at $\tau \to -\infty$, which is equal to 1 for $L=0$; in correspondence with the soliton center there will be a substantial depolarization of the material (which would be total in the ideal case $L=0$), followed by a change of sign of the original coherence when $\tau \to +\infty$.

In Figs. 2(c) and 2(f) we also show the phase space of the complex profiles of the solitary waves found numerically from Figs. 2(a) and 2(d).

Figure 3 shows the variation of the soliton area as defined by Eq. (35) as a function of parameter L, for four different values of soliton velocity v. Note the symmetric profile of this curve with respect to the axis $L=0$. This follows from the special discrete symmetry due to the simultaneous

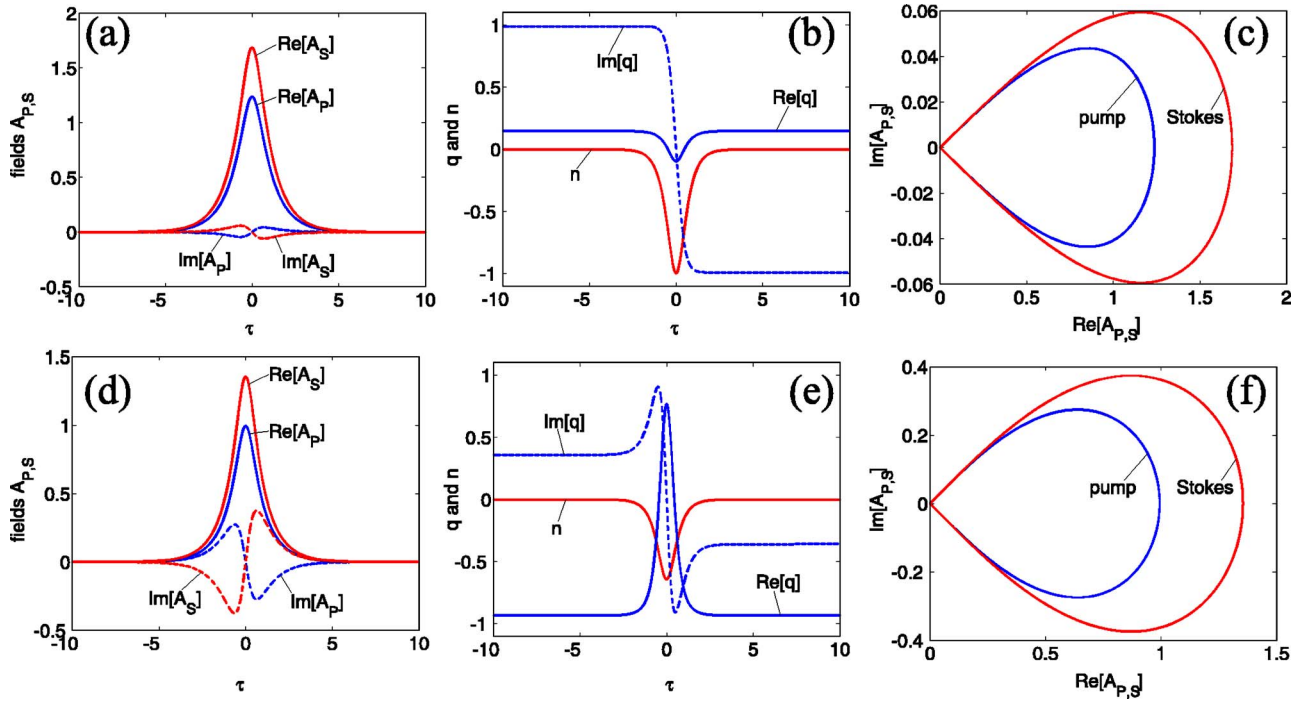

FIG. 2. (Color online) (a) Profiles of the hyperbolic secant soliton for parameters $v=0.3$ and $L=-0.4$. Blue (red) solid line: real part of A_P (A_S). Blue (red) dashed line: imaginary part of A_P (A_S). (b) Coherence q and population n for the soliton profiles shown in (a). The blue solid line is the real part of q, the blue dashed line is the imaginary part of q, and the red solid line is n. (c) Phase space of the complex soliton profiles shown in (a). The blue (red) line corresponds to A_P (A_S). (d), (e), (f) Same as (a), (b), (c), respectively, but for a relatively large value of the local-field parameter, $L=5$.

change of sign of L, $\mathrm{Im}(A_{P,S})$, and $\mathrm{Re}(q)$ in Eqs. (31)–(34), which has been already discussed. Thus, even if changing the sign of L would alter the physical meaning of this parameter as a dimensionless Debye shift, effectively there would be no modifications in the soliton dynamics that we are going to describe in this section.

It is evident that the pulse area for $|L|\neq 0$ is different from the value π, and it can change considerably for larger values of $|L|$. This is a natural consequence of the renormalization of the two-photon Rabi frequency contained in the Bloch equations (33) and (34). Finally, all the curves in Fig. 3 are

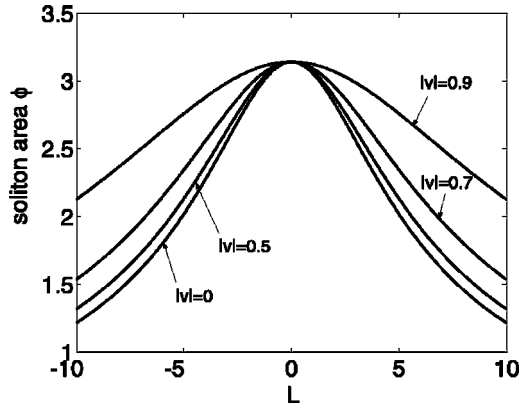

FIG. 3. Variation of the soliton area ϕ as defined by Eq. (35), found numerically by solving the BVP associated with Eqs. (31)–(34), as a function of L for four representative values of soliton velocity: $|v|=0$, $|v|=0.5$, $|v|=0.7$, and $|v|=0.9$.

independent of the sign of the parameter v, due to the invariance under the transformation $v\leftrightarrow -v$ and $a_{P,S}\leftrightarrow a_{S,P}$ in Eq. (39) and due to the use of the absolute value in the definition of ϕ in Eq. (35).

One distinguishing feature of the solitons under consideration is the existence of threshold values in energy and pulse duration for their formation (Fig. 4). In Fig. 4(a) the total dimensionless energy B, calculated numerically, is shown for three different values of L (see caption) as a function of the soliton parameter v; only a tiny variation of B with L is observed (see inset), which confirms the fact that a nonvanishing value of L mainly modifies the phase of the soliton, affecting only slightly the profile of the absolute value of the fields. This figure clearly shows the existence of a minimum value $B_{\min}$ for B in the soliton family, very close to the ideal (i.e., for $L=0$) value of 2π, below which no soliton can exist. The variation of the dimensionless pulse duration τ_0 with v of the stationary solutions found numerically is shown in Fig. 4(b), for the same three values of L used in Fig. 4(a). The value of τ_0 is calculated assuming a profile for $|A_{P,S}|$ very close to a functional form of the type $[\mathrm{sech}(\tau/\tau_0)]^{1/2}$ [15,16]. Here the three lines are coincident, and no soliton can exist with pulse duration greater than a certain $\tau_{\max}\simeq 1/2$. The estimate of the physical values corresponding to $B_{\min}$ and $\tau_{\max}$ for a realistic experimental configuration is a critical issue and will be discussed in more detail in Sec. V.

We have simulated the spatial propagation of an intense laser pulse in a InGaAsP QW with the specifics described in Sec. V, by using Eqs. (31)–(34). The initial pulse shape which is injected numerically into the QW is given by the following expressions:

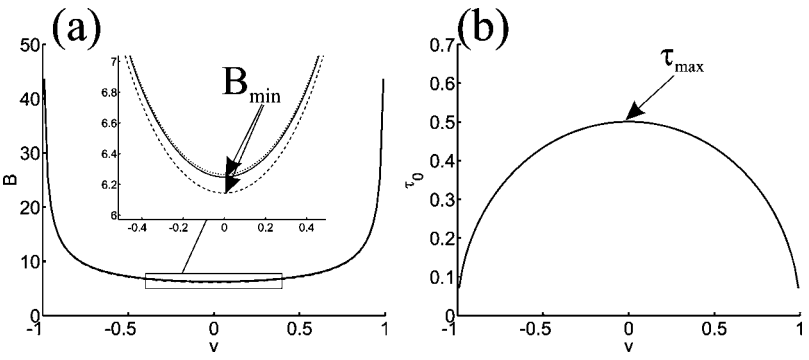

FIG. 4. (a) Total dimensionless energy B as a function of the soliton parameter v for three different values of L. Solid line: $L=-0.4$. Dotted line: $L=0$. Dashed line: $L=0.8$. The minimum excitation energy $B_{\min}$ is equal to the value 2π for $L=0$, and it is close to this value for $L\neq 0$. In the limits $v\rightarrow\pm 1$, the energy contained in the soliton diverges to infinity. (b) Pulse duration τ_0 of the soliton as a function of v, calculated numerically assuming a soliton profile for the absolute value of the amplitudes of the kind $[\mathrm{sech}(\tau/\tau_0)]^{1/2}$. In the limits $v\rightarrow\pm 1$, the soliton becomes indefinitely narrow. The curve is independent of L, and $\tau_{\max}=1/2$.

$$A_P=\Lambda\,\mathrm{sech}(f\tau),\quad A_S=\Lambda\nu\,\mathrm{sech}(f\tau), \tag{42}$$

where

$$\Lambda\equiv\left(\frac{fB}{2[1+\nu^2]}\right)^{1/2}. \tag{43}$$

The ratio between the Stokes and pump input peak amplitudes is regulated by ν. When $\nu=1$, the two initial components are launched with identical strengths. When $\nu\ll 1$ almost all energy is contained in the pump pulse A_P and no or small energy is carried by the Stokes pulse A_S. Exactly the opposite is true when $\nu\gg 1$. The slightly complicated normalization coefficient Λ given by Eq. (43) has the advantage that it always gives B as the total dimensionless energy for the two components given by Eq. (42), irrespective of ν, so that one can use B and ν as two independent control parameters to explore numerically the dynamics of the propagation. The factor $f=1.76$ is chosen to match the common experimental practice of specifying the full width at half maximum (FWHM) of the pulse [28].

Maxwell's equations (31) and (32) have been solved using the split-step Fourier method [28], while for Bloch's equations (33) and (34) we have used an Adams-Moulton implicit algorithm in order to improve the temporal precision, with the advantage that our code is able to simulate with sufficient accuracy relatively long propagation distances, if compared to more conventional algorithms such as the fourth-order Runge-Kutta method. For our representative numerical results we have chosen the value $L=-0.4$ for the local-field parameter and $\gamma_1=\gamma_2\simeq 0.17$ for the dephasing parameters, which correspond to $T_1=T_2\simeq 1$ psec, for a pulse duration of $t_0\simeq 200$ fsec. A discussion of the origin of the above parameters is given in Sec. V, and a brief review of the dynamics for other values of the parameter L is given at the end of this section.

The most important dynamics is observed when $\nu\ll 1$—i.e., when almost all the input energy is contained into a single initial pulse, which is tuned at the pump frequency ω_P—i.e., at the transition frequency between the LH valence band and the CB at the Γ point. Under these conditions one can observe the soliton formation if energy B is above the threshold value, $B>B_{\min}\simeq 2\pi$ in dimensionless units. In Fig. 5(a) the initial (dotted line) and final (solid line and dashed lines) field amplitudes after a propagation of $\xi=15$ are shown. The initial pulse undergoes temporal compression, necessary to overcome the threshold in pulse duration imposed by the maximum of the curve shown in Fig. 4(b). Together with the pulse compression, the Stokes wave A_S, which initially was not excited in the system, grows

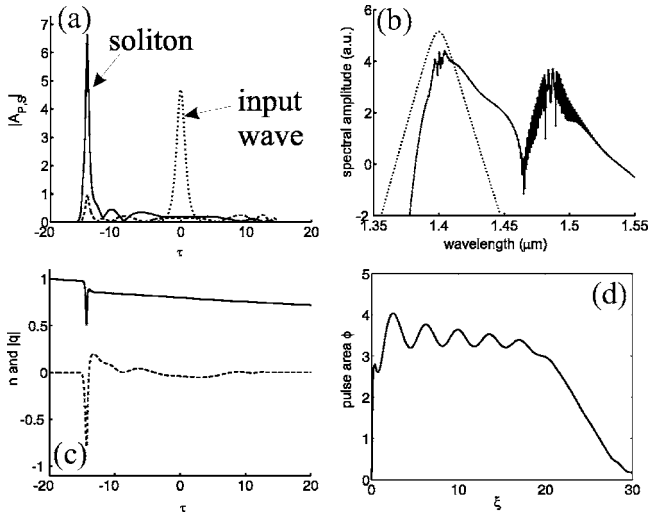

FIG. 5. (a) Snapshot of field amplitudes at $\xi=0$ (dotted line) and $\xi=15$ (dashed line, Stokes wave; solid line, pump wave), when the QW is pumped with a single field tuned at $\lambda_P=1.4$ μm, with dimensionless energy $B=25$ (corresponding to a physical energy flux of 104 J/m^2) and $\nu=10^{-12}$ in Eqs. (42) and (43). (b) Spectral amplitude at $\xi=0$ (dotted line) and $\xi=15$ (solid line), in the same pumping conditions of (a), showing the spontaneous growth of the Stokes wave at $\lambda_S=1.48$ μm from the background noise. Vertical scale is logarithmic. (c) Snapshot of the population field n (dashed line) and the coherence field $|q|$ (solid line) for $\xi=15$, in the same pumping conditions of (a), showing the typical functional behavior of the solitary wave of Eqs. (39)–(41). Depolarization and population inversion are not complete in correspondence with the soliton center, due to the presence of decoherence processes in the Bloch part of the equations [$\gamma_{1,2}\simeq 0.17$ in Eqs. (33) and (34)] and a nonvanishing value of L [see Figs. 2(b) and 2(e)]. The overall decay of the polarization is due to the dephasing term proportional to $1/T_2$ in Eq. (27). (d) Pulse area evolution during spatial propagation. Launching parameters are the same as in (a), (b), (c). The soliton is well formed for $\xi=15$ [see (a), (b), and (c)], but due to gradual loss of coherence, the two components unlock at $\xi\simeq 20$, and correspondingly the pulse area falls to zero.

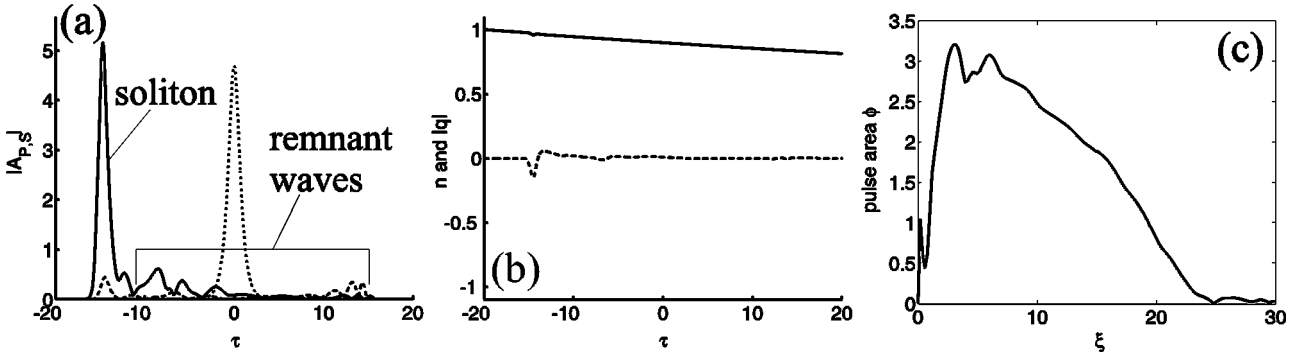

FIG. 6. (a) Snapshot of field amplitude at $\xi=0$ (dotted line) and $\xi=15$ (dashed line, Stokes wave; solid line, pump wave), in the same pumping conditions of Fig. 5, but with $L=5$. This relatively large value of L produces oscillating waves on the right of the soliton, which prove to be detrimental for the soliton propagation and lead to a rapid decay of the solitary wave. (b) Snapshot of the population field n (dashed line) and the coherence field $|q|$ (solid line) for $\xi=15$, in the same pumping conditions and parameters as in (a). The population inversion in correspondence with the soliton peak is very mild, and the polarization change in the material near the soliton center is very small. The overall decay of the polarization is due to the dephasing term proportional to $1/T_2$ in Eq. (27). (c) Pulse area evolution during spatial propagation, in the same conditions as in (a) and (b). After reaching a maximum at around $\xi\simeq 3$, the pulse area goes down steadily, which is an indication of soliton decay.

spontaneously until it reaches a certain saturation value, determined by the soliton velocity; see also the expressions for $a_{P,S}$ given after Eqs. (39)–(41). This phenomenon is clearly shown in Fig. 5(b), where the spectral amplitudes of the total electric field for $\xi=0$ and $\xi=15$ are plotted. The Stokes field, the amplitude of which was at the background noise level at $\xi=0$, grows spontaneously very quickly during propagation, saturating at a level determined by the final soliton velocity. After a propagation distance of $\xi\simeq 15$ [solid and dashed lines in Fig. 5(a)], the soliton is well formed, together with some slower remnant waves, the energy of which did not manage to lock into the soliton. For $\xi>20$ the solitary wave propagates for some appreciable distance, but eventually the cumulative effect of the dephasing processes prevails and the pump wave reduces its amplitude continuously, with the consequent final unlocking of the two components. This determines a soliton "lifetime," strongly dependent on the precise values of $\gamma_{1,2}$ and less strongly on the spectral dependence of the absorption coefficients $\alpha_{P,S}(\omega)$.

In Figure 5(d) the evolution of the pulse area [Eq. (35)] with ξ during the soliton formation is also shown. From its initial arbitrary value, ϕ oscillates around a value of just below π, which is the natural pulse area of the hyperbolic secant solitons considered here for $L=0$ [15,16]; see also Eqs. (39)–(41) and Fig. 3. However, at a propagation distance of about $\xi\simeq 20$, the soliton dies out and the two components no longer travel at the same common velocity, with the consequent fall of the pulse area to zero.

Figure 5(c) shows a snapshot of the absolute value of the coherence field $|q|$ and the population n for $\xi=15$, showing that in correspondence with the soliton maximum $|q|$ and n have the functional behavior expected from Eqs. (39)–(41).

A completely different evolution of light is observed numerically in the complementary case $\nu\gg 1$ (not shown here)—i.e., when almost all energy is concentrated into the Stokes wave A_S. Despite this apparently insignificant change in the pumping conditions, the pump component never manages to grow from the background and the soliton is never formed.

Finally, it is necessary to discuss the influence of other values (and sign) of the local-field parameter L on the dynamics of propagation, but still within the case $\nu\ll 1$. First of all it must be said that the salient features of the simulation, such as output spectra and absolute values of all fields of interest, are independent of the sign of L, due to the symmetry mentioned in Sec. III. For L close to zero, we obviously recover the "ideal" case of the solitons of Kaplan *et al.*, with real profiles, the dynamics of which has already been discussed extensively in Ref. [16]. Increasing the magnitude of $|L|$, nonsolitonic waves are continuously generated just on the right of the soliton, on the retarded part of the time axis. These remnant waves are detrimental to the soliton propagation and lead to an additional source of destabilization for the solitary wave. In Fig. 6(a) the amplitudes $|A_{P,S}|$ for $\xi=15$ are shown for a simulation with parameters and input conditions exactly analogous to the simulation performed in Fig. 5, but for a relatively large value of the local-field parameter, $|L|=5$. Figure 6(b) shows the population and coherence fields at $\xi=15$, and one can see that only a small and very partial population "inversion" occurs in correspondence with the soliton peak, while there is an unnoticeable change in the polarization of the material. Also, it is evident in Fig. 6(c), where the evolution of the pulse area during the propagation is shown, that the pulse area reaches a maximum at $\xi\simeq 3$, but steadily goes down with propagation, which is an indication of the soliton destabilization and decay.

In conclusions, large values of $|L|$ lead to a more confusing solitons dynamics, due to the generation of remnant waves from the input pulse.

IV. CONTINUUM GENERATION IN DOUBLE-PUMPING CONDITIONS

When the QW is pumped with both pump and Stokes fields with comparable intensity ($\nu\sim 1$), the development of a relatively broad frequency continuum in the semiconductor can be observed in the simulations. It has been recently

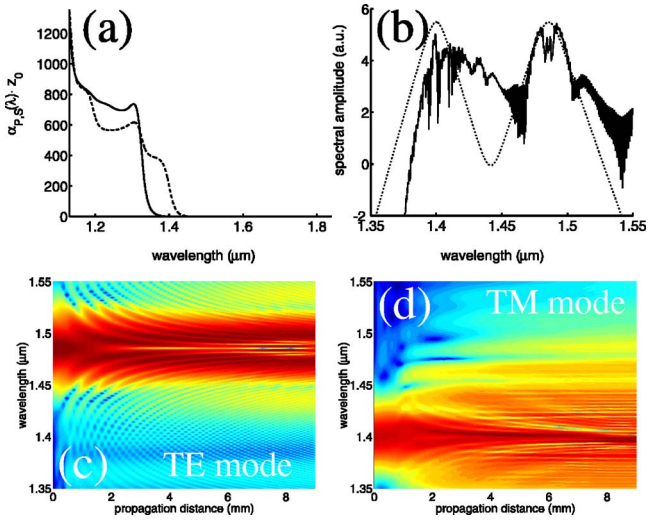

FIG. 7. (Color online) (a) Absorption spectra for TE (dotted line) and TM (solid line) modes, shown in dimensionless units $\alpha_{P,S}(\omega)z_0$, as calculated using momentum matrix elements derived from $k\cdot p$ theory [38]. (b) Generation of an optical continuum from a InGaAsP QW pumped with two input fields with equal amplitude, $\nu=1$. On the vertical axis (in logarithmic scale) the spectral amplitude in arbitrary units is shown. $\lambda_P=1.4$ μm, $\lambda_S=1.48$ μm, and $t_0=200$ fsec. The total dimensionless energy is $B=100$, corresponding to a physical energy flux of 420 J/m^2. Dashed line: initial spectrum. Solid line: spectrum after a propagation of $\xi=15$, corresponding to 9 mm, using the specifics proposed in Sec. V. (c) Evolution of the optical field in the TE polarization as a function of propagation distance, in the same conditions of (a) and (b). color scale is logarithmic. (d) Same as (c) but for the TM polarization.

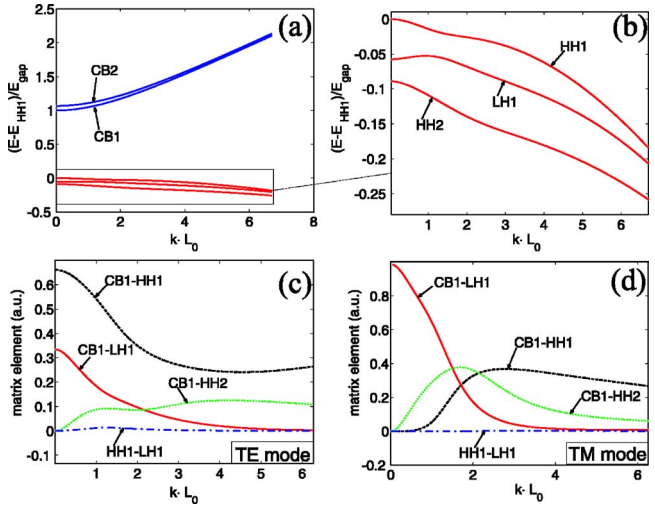

FIG. 8. (Color online) (a) Band structure of the InGaAsP QW considered in Sec. V, calculated for room temperature. All energies are shifted by the arbitrary value E_{HH1}, which is the physical energy of the HH1 band at the Γ point [see also Fig. 1(a)]. (b) Enlargement of the valence band structure of (a). (c) Dipole matrix elements for the optical transitions between the relevant bands, TE mode. Matrix elements corresponding to different transitions (CB1-HH1, black dashed line; CB1-LH1, red solid line; CB1-HH2, green dotted line; HH1-LH1, blue dash-dotted line) are indicated with arrows. (d) Same as (c) but for the TM mode.

shown in the literature (both numerically and experimentally) that the appearance of a supercontinuum in optical fibers is mainly due to multiple-soliton generation and -soliton splitting, which give rise to an explosive nonlinear evolution and the consequent generation of light in a broad range of frequencies [35]. The continuum is broader and flatter in frequency space when the optical fiber is pumped with ultrashort, femtosecond light pulses and under anomalous dispersion conditions, where the formation of multiple solitons is favorable [16,35].

We have simulated the propagation of two pulses in the QW tuned at ω_P and ω_S, respectively. The resulting spectrum after a spatial propagation of 15 dispersion lengths (corresponding to 9 mm for the specific configuration and materials described in Sec. V) is reproduced in Fig. 7(b). The initial spectrum is indicated with a dashed line and the final spectrum with a solid line; the spectral amplitudes are represented by a logarithmic scale on the vertical axis. The total dimensionless energy of the input pulses was $B=100$ (corresponding to a physical total energy flux of 420 J/m^2), and the FWHM of pump and Stokes was taken to be $t_0=200$ fsec. An appreciable continuum generation spanning more than 200 nm is observed. Figure 7(a) shows the absorption spectra for the pump wave (TM mode, solid line) and for the Stokes wave (TE mode, dashed line), as calculated using a free-carrier approximation for the band structure (see also Sec. V for further explanations). Also, the polarization of the continuum is shown in Figs. 7(c) and 7(d), where a contour plot of the evolution of the optical fields as a function of propagation distance is given for the two polarization states.

Future studies will determine quantitatively the degree of phase coherence of the continua of the kind shown in Fig. 7(b) generated by resonant solitons in QW's, as opposed to the ones generated by off-resonance nonlinearities which act in optical fibers [35].

V. PROPOSED GEOMETRY AND MATERIALS

Here we propose an experimental configuration and a material composition for the QW and surrounding barrier, for which the approximations used throughout the text are reasonably valid. Numerical values of the parameters calculated in this section have been used in all the simulations of Secs. III and IV.

The structure considered is based on the InGaAsP material system (composition of the well, 56% In, 44% Ga, 95% As, 5% P; composition of the barrier, 79% In, 21% Ga, 45% As, and 55% P). The width of the well is $L_0=45$ Å.

In Fig. 8(a) the band structure of the QW considered above is shown, as calculated using an eight-band $k\cdot p$ theory [36] and using material parameters from Ref. [37]. The energy of the bands is shown on the vertical axis, normalized with the gap energy E_{gap} [i.e., the energy separation between the HH1 band and the CB1 band at the Γ point in Fig. 8(a)], while on the horizontal axis the parallel wave vector k is shown, normalized with the well width L_0. For this structure $E_{\mathrm{gap}}=0.886$ eV, which corresponds to the optical wavelength

$\lambda_S = 1.48\ \mu$m. The energy separation between the LH1 band and CB1 band at the Γ point corresponds to the wavelength $\lambda_P = 1.4\ \mu$m. The separation between the HH1 band and LH1 band is calculated to be $\epsilon_{12} = 51$ meV, which corresponds to 12.36 THz in frequency. The condition $\epsilon_{12} \ll E_{\text{gap}}$ is therefore well satisfied, and the decoupling of the CB1 from the LH1-HH1 system described by Eqs. (16) and (17) represents an excellent approximation.

The calculated material refractive index at λ_P is $n_P \simeq 3.681$, and the index at λ_S is $n_S \simeq 3.652$. The superficial density of carriers is assumed to be $N_{2d} \simeq 8.5 \times 10^{14}$ particles/m^3, corresponding to a volume density of $N_{3d} \simeq 1.8 \times 10^{23}$ particle/m^3. The coefficient which appears in the scaling of the optical fields in Eq. (30) has the value $\tilde{\alpha}^{1/2} \simeq 5.4 \times 10^7$ V/m and $\kappa = 0.05$ for $\Delta\beta' \simeq 0.1/c$. This latter value for $\Delta\beta'$ is calculated from the waveguide dispersion of the slab created by the QW and the barriers in Fig. 1(b). The common value of γ_P/n_P and γ_S/n_S used in Eqs. (25) and (26) is $\simeq 460$ m^{-1}. The temporal scale used to scale time in Eqs. (29) is given by $t_0 \simeq 200$ fsec. It follows that the threshold value for the soliton width is $t_{\max} = \tau_{\max} t_0 \simeq 100$ fsec, so that an initial pulse will be compressed below this value before locking to a solitary wave.

The Debye shift $\mathcal{V}$ for this structure and materials is estimated by using standard expressions for the screened-exchange and Coulomb-hole self-energy (see, for instance, pp. 98–99 of [19], and [33]). Here we use the value $\mathcal{V} \simeq -10$ meV, which gives $L \simeq -0.4$ if using $t_0 \simeq 200$ fsec as reference pulse duration. Also, the dipole moment $|\mathbf{d}|$ used in the expressions for the Rabi frequencies is $|\mathbf{d}| \simeq 6$ Å $\times e_0$, where e_0 is the electron electric charge.

The relative strength of the optical transitions between the various bands are shown in Figs. 8(c) and 8(d), respectively, for the TE and TM modes propagating in the QW. From these latter figures it is possible to deduce the optimal polarization for the pump and Stokes fields. The transition between the CB1 and LH1 levels is stronger around the Γ point if the field associated with this transition is TM polarized, as can be seen from the red solid line of Fig. 8(d). At the same time, for the same polarization, the transition strength between CB1 and HH1 is relatively weak with respect to CB1-LH1, at least for a region of wave vectors localized around $k \cdot L_0 \simeq 0$; see the black dashed line in Fig. 8(d). On the other hand, the transition strength between CB1 and HH1 is favored if the field associated with this transition is TE polarized, while the transition is less intense if the TE polarization is chosen for the CB1-LH1 transition. We can therefore conclude that the logical configuration corresponds to the pump field (A_P, at λ_P) TM polarized and the Stokes field (A_S, at $\lambda_S > \lambda_P$) TE polarized. The same conclusion can be drawn from analyzing the strength of the transitions in Fig. 8(c). It is also important to note that the intervalence dipole transition strength between HH1 and LH1 in the two polarizations is very small and negligible with respect to the other transitions [see the blue dash-dotted lines in Figs. 8(c) and 8(d)], which makes the intervalence band transition physically very similar to a Raman process [15,16]. Figure 7(a) shows the free carrier absorption spectra for the TE and TM modes, as calculated using the $k \cdot p$ momentum matrix elements [38] and with a hyperbolic secant broadening introduced of width 6.6 meV.

The coherent preparation of the QW hole population can be induced using experimental techniques similar to those used for molecular systems; see also [39] and references therein.

It has been demonstrated numerically in Sec. III that, for the parameters given there, dimensionless propagation distances of the order of 10 dispersion lengths are necessary to observe the soliton formation; see also Fig. 5 and caption. Choosing the reference pulse duration as $t_0 \simeq 200$ fsec, the first-order dispersion length will be of the order of $z_0 \simeq 0.6$ mm. This already indicates that observation of solitary waves with the proposed geometry and materials can only occur if the physical propagation distance is at least 5 mm or greater. As a consequence, we consider here only the *in-plane* geometry—i.e., when the propagation of light is parallel to the plane of the QW—instead of the traditional normal incidence configuration [see Fig. 1(b) and caption].

Finally, and most importantly, the threshold energy flux for soliton generation must be estimated. In dimensionless units this energy is given by $B \simeq 2\pi$; see Eqs. (39)–(41) and Fig. 4(a). In physical units this corresponds to the value $\mathcal{F} \simeq 26$ J/m^2.

VI. CONCLUSIONS

In this paper we have investigated numerically the possibility for the physical excitation in InGaAsP QW's of a special class of one-parameter solitons, first discovered theoretically by Kaplan *et al.* in the different context of Raman cells filled with a Raman-active gas [15] and further developed in the strongly dispersive case of hollow-core photonic crystal fibers in Refs. [16,17]. Following a procedure analogous to that of Ref. [31], we have first derived a set of effective equations for the macroscopic observables q and n [Eqs. (31)–(34)] from the semiconductor Bloch equations [Eqs. (7)–(13)], using a phenomenological reduction which makes use of the Debye shift to quantify the local electric field due to many-body renormalization effects.

The preparation of the QW in a state where the $|\text{LH}\rangle$ and $|\text{HH}\rangle$ bands are initially populated with an equal number of holes permits the excitation of solitons with a hyperbolic secant profile, which are in principle very difficult to excite in atomic 3LS's. The thresholds in pulse energy and pulse duration have been also determined. Detailed numerical simulations have shown that the soliton can be efficiently generated by launching a strong pulse at the resonance frequency between the LH band and CB band at the Γ point; the conditions of low temperature will increase the soliton lifetime considerably.

Finally, in the numerical simulations we have found that by launching the pump pulse and the Stokes pulse together with equal or similar intensity, a continuum of at least a 200-nm bandwidth can be generated efficiently in a few millimeters of propagation.

We conclude that further exploration of the nonlinearities which occur in resonant multiphoton transitions in semiconductor materials may lead to the discovery of the existence of completely new and unconventional solitary waves, of the kind described in the present paper.

ACKNOWLEDGMENTS

One of the authors (F.B.) acknowledges D.V. Skryabin of the University of Bath (UK) and A.L. Ivanov and C. Creatore of the University of Cardiff (UK) for early discussions. This research has been supported by Science Foundation Ireland (SFI).

[1] D. S. Chemla and J. Shah, Nature (London) **411**, 549 (2001).
[2] L. Allen and J. H. Eberly, *Optical Resonance and Two-Level Atoms* (Wiley, New York, 1975).
[3] L. Schultheis *et al.*, Appl. Phys. Lett. **47**, 995 (1985).
[4] S. T. Cundiff *et al.*, Phys. Rev. Lett. **73**, 1178 (1994); A. Schulzgen *et al.*, *ibid.* **82**, 2346 (1999); H. Giessen *et al.*, *ibid.* **81**, 4260 (1998).
[5] A. Mysyrowicz *et al.*, Phys. Rev. Lett. **56**, 2748 (1986); A. von Lehmen *et al.*, Opt. Lett. **11**, 609 (1986); B. Fluegel *et al.*, Phys. Rev. Lett. **59**, 2588 (1987).
[6] S. L. McCall and E. L. Hahn, Phys. Rev. Lett. **18**, 908 (1967); Phys. Rev. **183**, 457 (1969).
[7] I. Talanina, J. Opt. Soc. Am. B **13**, 1308 (1996); Phys. Lett. A **241**, 179 (1998); I. Talanina, D. Burak, R. Binder, H. Giessen, and N. Peyghambarian, Phys. Rev. E **58**, 1074 (1998).
[8] C. R. Stroud, Jr. *et al.*, Opt. Commun. **67**, 387 (1988); H. Giessen *et al.*, Phys. Rev. Lett. **81**, 4260 (1998); N. C. Nielsen *et al.*, Phys. Rev. B **64**, 245202 (2001); A. A. Afanas'ev *et al.*, J. Opt. Soc. Am. B **19**, 911 (2002); N. C. Nielsen *et al.*, Phys. Rev. Lett. **94**, 057406 (2005).
[9] S. E. Harris, Phys. Rev. Lett. **62**, 1033 (1989); E. S. Fry *et al.*, *ibid.* **70**, 3235 (1993); G. G. Padmabandu *et al.*, *ibid.* **76**, 2053 (1996).
[10] S. E. Harris, Phys. Rev. Lett. **77**, 5357 (1996); G. Z. Zhang, K. Hakuta, and B. P. Stoicheff, *ibid.* **71**, 3099 (1993).
[11] J. Oreg, F. T. Hioe, and J. H. Eberly, Phys. Rev. A **29**, 690 (1984); B. W. Shore, K. Bergmann, J. Oreg, and S. Rosenwaks, *ibid.* **44**, 7442 (1991); S. E. Harris, Phys. Today **50**(7), 36 (1997).
[12] L. V. Hau *et al.*, Nature (London) **397**, 594 (1999).
[13] K. B. Ferrio and D. G. Steel, Phys. Rev. Lett. **80**, 786 (1998); M. Joschko *et al.*, *ibid.* **78**, 737 (1997); R. Binder *et al.*, Phys. Status Solidi B **221**, 169 (2000); M. E. Donovan *et al.*, Phys. Rev. Lett. **87**, 237402 (2001); I. Rumyantsev, N. H. Kwong, R. Takayama, and R. Binder, Phys. Rev. B **65**, 245325 (2002).
[14] D. D. Yavuz, D. R. Walker, and M. Y. Shverdin, Phys. Rev. A **67**, 041803(R) (2003); D. V. Skryabin, F. Biancalana, D. M. Bird, and F. Benabid, Phys. Rev. Lett. **93**, 143907 (2004).
[15] A. E. Kaplan *et al.*, Opt. Lett. **19**, 445 (1994); A. E. Kaplan, Phys. Rev. Lett. **73**, 1243 (1994); A. E. Kaplan and P. L. Shkolnikov, J. Opt. Soc. Am. B **13**, 347 (1996).
[16] F. Biancalana, Ph.D. thesis, University of Bath, UK, 2005, Chap. 4.
[17] D. V. Skryabin, A. V. Yulin, and F. Biancalana, Phys. Rev. E **73**, 045603(R) (2006).
[18] C. Klingshirn, *Semiconductor Optics*, 2nd ed. (Springer-Verlag, Berlin, 2005).
[19] W. W. Chow and S. W. Koch, *Semiconductor-Laser Fundamentals* (Springer-Verlag, Berlin, 1999).
[20] J. Reintjes and M. Bashkansky, in *Handbook of Optics*, edited by M. Bass (McGraw-Hill, New York, 2001), Vol. IV, Chap. 18.
[21] H. Haug and S. W. Koch, *Quantum Theory of the Optical and Electronic Properties of Semiconductors*, 2nd ed. (World Scientific, Singapore, 1993).
[22] J. M. Luttinger and M. Kohn, Phys. Rev. **97**, 869 (1955); J. M. Luttinger, *ibid.* **102**, 1030 (1956).
[23] R. Binder and M. Lindberg, Phys. Rev. B **61**, 2830 (2000); R. Binder *et al.*, in *Coherent Optical Interactions in Semiconductors*, edited by R. T. Phillips, Vol. 330 of *NATO of Advanced Study Institute, Series B: Physics* (Plenum Press, New York, 1994), p. 63.
[24] *Nonlinear Optics in Semiconductors I, Semiconductors and Semimetals*, edited by E. Garmire (Academic Press, San Diego, 1999), Vol. 58.
[25] A. Knorr, R. Binder, M. Lindberg, and S. W. Koch, Phys. Rev. A **46**, 7179 (1992).
[26] J. Shah, *Ultrafast Spectroscopy of Semiconductors and Semiconductor Nanostructures*, 2nd ed. (Springer-Verlag, Berlin, 1999).
[27] R. R. Puri, *Mathematical Methods of Quantum Optics* (Springer-Verlag, Berlin, 2001).
[28] Y. S. Kivshar and G. P. Agrawal, *Optical Solitons* (Academic Press, San Diego, 2003).
[29] M. Lindberg and S. W. Koch, Phys. Rev. B **38**, 3342 (1988).
[30] K. Victor *et al.*, Z. Phys. B: Condens. Matter **99**, 197 (1996); K. Victor, V. M. Axt, and A. Stahl, Phys. Rev. B **51**, 14164 (1995).
[31] C. M. Bowden and G. P. Agrawal, Opt. Commun. **100**, 147 (1993); G. P. Agrawal and C. M. Bowden, IEEE Photonics Technol. Lett. **5**, 640 (1993); C. M. Bowden and G. P. Agrawal, Phys. Rev. A **51**, 4132 (1995); J. Yao *et al.*, Opt. Commun. **119**, 246 (1995).
[32] J. M. Shacklette and S. T. Cundiff, Phys. Rev. B **66**, 045309 (2002); M. Wegener, D. S. Chemla, S. Schmitt-Rink, and W. Schafer, Phys. Rev. A **42**, 5675 (1990); C. M. Bowden and J. P. Dowling, *ibid.* **47**, 1247 (1993); A. L. Smirl, M. J. Stevens, X. Chen, and O. Buccafusca, Phys. Rev. B **60**, 8267 (1999).
[33] H. Haug and S. W. Koch, Phys. Rev. A **39**, 1887 (1989).
[34] Q-H. Park and H. J. Shin, e-print hep-th/9505017; e-print hep-th/9506087; e-print hep-th/9509120; e-print hep-th/9605052; e-print hep-th/9606094; I. Bakas, Q-Han Park, and H. J. Shin, e-print hep-th/9512030.
[35] A. V. Husakou and J. Herrmann, Phys. Rev. Lett. **87**, 203901 (2001); J. Herrmann *et al.*, *ibid.* **88**, 173901 (2002); X. Gu *et al.*, Opt. Express **11**, 2697 (2003), http://www.opticsexpress.org/abstract.cfm?URI=OPEX-11-21-2697
[36] E. O. Kane, Semicond. Semimetals **1**, 75 (1966).
[37] C. G. Van de Walle, Phys. Rev. B **39**, 1871 (1989); I. Vurgaftman *et al.*, J. Appl. Phys. **89**, 5815 (2001).
[38] F. Szmulowicz, Phys. Rev. B **51**, 1613 (1995); F. Szmulowicz and G. Brown, Appl. Phys. Lett. **66**, 1659 (1995).
[39] J. J. Baumberg *et al.*, J. Opt. Soc. Am. B **13**, 1246 (1996); A. P. Heberle *et al.*, Phys. Rev. Lett. **75**, 2598 (1995); A. V. Sokolov *et al.*, *ibid.* **85**, 562 (2000).